Heterogeneously integrated 2.0 μm CW hybrid silicon lasers at room temperature

Alexander Spott,[1,*] Michael Davenport,[1] Jon Peters,[1] Jock Bovington,[1] Martijn J. R. Heck,[1] Eric J. Stanton,[1] Igor Vurgaftman,[2] Jerry Meyer,[2] and John Bowers[1]

[1]*Department of Electrical and Computer Engineering, University of California, Santa Barbara, Santa Barbara, California 93106, USA*

[2]*Naval Research Laboratory, Washington, DC 20735, USA*

**Corresponding author: spott@ece.ucsb.edu*

Received January 19, 2015; revised February 20, 2015; accepted February 24, 2015; posted March 3, 2015 (Doc. ID 232163); published March 27, 2015

Here we experimentally demonstrate room temperature, continuous-wave (CW), 2.0 μm wavelength lasers heterogeneously integrated on silicon. Molecular wafer bonding of InP to Si is employed. These hybrid silicon lasers operate CW up to 35°C and emit up to 4.2 mW of single-facet CW power at room temperature. III–V tapers transfer light from a hybrid III–V/silicon optical mode into a Si waveguide mode. These lasers enable the realization of a number of sensing and detection applications in compact silicon photonic systems. © 2015 Optical Society of America

OCIS codes: (140.5960) Semiconductor lasers; (140.3070) Infrared and far-infrared lasers; (130.3120) Integrated optics devices; (130.0250) Optoelectronics.

http://dx.doi.org/10.1364/OL.40.001480

Long-wavelength optoelectronic devices on silicon are important for low cost and high levels of integration [1]. The mid-infrared regime, 2–20 μm, is of particular interest for a variety of sensing and detection applications. Many of these will benefit from the low cost, compact device size, and commercial scalability enabled by integration in a silicon photonics platform. Chemical bond spectroscopy [2], biological sensing and diagnostics (lab-on-a-chip) [3], thermal imaging, gas detection [4], environmental monitoring, and oceanographic sensing are all important applications for silicon mid-infrared devices. Additionally, the 2–3 μm spectral region is known to be advantageous for on-chip nonlinear optics for the amplification and generation of light [5,6], in part due to reduced two-photon absorption in silicon at longer wavelengths.

However, room-temperature CW on-chip sources emitting at mid-infrared wavelengths are needed to realize these applications. A number of mid-infrared silicon devices on various material systems have already been demonstrated, including waveguides, resonators [7], photonic crystal cavities [8], arrayed waveguide gratings [9], and couplers [10]. A pulsed, room temperature, hybrid silicon laser operating at 1.9 μm has been reported [11], as well as preliminary results of a 2.38 μm, polymer-adhesive-bonded, pulsed hybrid silicon laser operating at 10°C [12]. Here we demonstrate 2.0 μm hybrid silicon lasers operating CW up to 35°C and heterogeneously integrated with silicon waveguides.

The hybrid silicon design is based on previous laser results at wavelengths from 1310 to 1600 nm. Figure 1(a) shows a schematic cross-section of the laser gain region, where a broad-area III–V mesa is bonded onto the silicon waveguide. The hybrid optical mode is laterally confined by the silicon waveguide, while a portion of the mode overlaps the III–V multiple quantum well (MQW) active region. The confinement factor in the III–V active region depends on the silicon waveguide dimensions. Figure 1(b) shows simulated optical modes for various waveguide widths, along with corresponding estimated confinement factors in the quantum well region.

The III–V mesa is terminated on both sides by a lateral tapering of the III–V material to a point, causing the hybrid active mode to couple into a passive silicon waveguide mode. A Fabry–Pérot cavity is then formed by the polished silicon facets. Figure 1(c) shows a top view of the laser layout.

A MQW laser diode structure with four InGaAs quantum wells was modified to be suitable for hybrid silicon integration. This structure was epitaxially grown with metalorganic chemical vapor deposition (MOCVD) on an InP substrate by nLight.

The devices were designed with either 1 or 2 mm-long active hybrid silicon/III–V sections. The p-InGaAs contact layer, cladding layers, separate confinement heterostructure (SCH) layers, and active layers were tapered over a

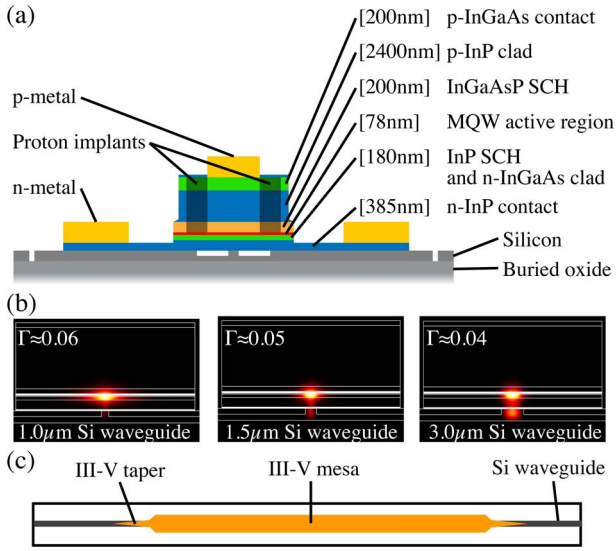

Fig. 1. (a) Cross-sectional schematic of hybrid silicon active region with approximate layer thicknesses. Some III–V layers, such as growth transition regions, are not shown. (b) Simulated optical mode profiles and estimated MQW optical confinement factor of hybrid silicon active region for various silicon waveguide widths. (c) Top view schematic of hybrid laser design.

20 μm length, while the lower n-InP contact was tapered in a separate short transition. In most devices, the III–V mesa was 24 μm wide, and proton implantation was used to form a current channel to prevent current spreading and ensure overlap of the carriers with the optical mode. Lasers with 2-mm-long active regions had current channels ranging from 4 to 6 μm wide. Lasers with 1-mm-long active regions had only 4-μm-wide current channels, and some employed a narrower (4–12 μm) III–V mesa. Mesas of width 6 μm or less were not implanted.

The silicon-on-insulator (SOI) wafer had a 500 nm silicon device layer with a 1 μm buried oxide underneath. The top silicon was etched halfway to form rib waveguides with widths ranging from 0.5 to 3 μm in the hybrid active region. Thinner waveguides were widened to 2 μm underneath the III–V taper sections. Waveguides in the passive silicon section were 0.8 μm wide for most devices. In the remainder of this Letter, references to the silicon waveguide width correspond to the silicon waveguides underneath the III–V mesas.

Figure 2 illustrates a simplified process flow diagram. A $CF_4/SF_6/Ar$ inductively coupled plasma (ICP) dry etch defined the silicon waveguides. The actual waveguide etch depth was measured to be about 235–240 nm. To aid in bonding, vertical channels were etched through the silicon device layer to the buried oxide [13].

The III–V material was bonded to the SOI by plasma-assisted wafer bonding, followed by annealing at 300°C for 60 min [14]. The InP substrate was removed by mechanical lapping and a 3:1 $HCl:H_2O$ wet etch that stopped at a 50 nm InGaAs etch stop layer. III–V mesas were defined in three steps. First, the mesas were etched with a methane–hydrogen–argon (MHA) recipe in a reactive-ion etcher (RIE), and stopped near the bottom of the p-InP cladding layer. Second, in order to improve the etch-depth uniformity, an intermediate selective 1:3 $HCl:H_3PO_4$ wet etch step was used to remove any remaining InP and leave a level InGaAsP surface. Third, another MHA step etched through the active region and stopped in the n-InP contact layer. Pd/Ge/Pd/Au was deposited on the n-InP to form bottom contacts, and Pd/Ti/Pd/Au was deposited on the p-InGaAs to form top contacts. Current channels, seen in Fig. 1(a), were formed by proton implantation with energies ranging from 10 to 260 keV.

The fabricated dies were diced into laser bars, and the silicon facets were polished but not coated. The resulting Fabry–Perot cavities contained passive silicon waveguide regions of length 450–650 μm on each side of the active hybrid mesas. A top-down optical microscope image of a fully fabricated laser bar and the III–V taper can be seen in Fig. 3.

The laser bars were mounted with thermal paste on a copper block for testing. The temperature was maintained with a thermoelectric cooler and water-cooling system. An integrating sphere and Thorlabs detector (DET10D) were used to capture the light and measure the output power. The measurements were calibrated by focusing light from one device through an NA = 0.85 aspherical lens directly onto the DET10D detector. Because the coupling loss could not be precisely determined, the absolute power produced by the lasers may be slightly higher than the reported values.

A total of 50 lasers were measured. Figure 4 shows the output power versus current characteristics for a laser

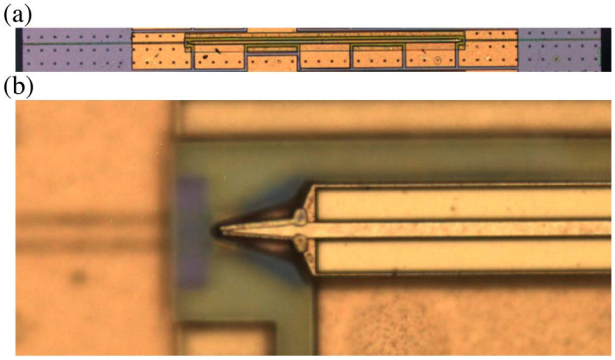

Fig. 3. (a) Optical microscope image of a fully-fabricated laser with a 1-mm-long III–V mesa. (b) Close-up microscope image of a laser's III–V taper region.

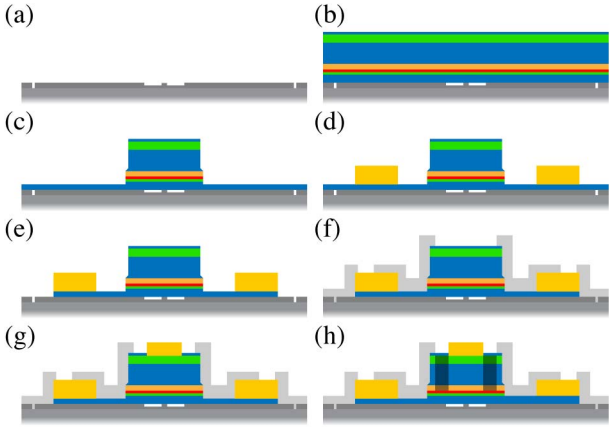

Fig. 2. Process flow: (a) Silicon waveguide and vertical channel etch. (b) III–V bonding and substrate removal. (c) Mesa dry and wet etch steps. (d) n-Metal deposition. (e) n-InP etch. (f) SiO_2 deposition and via etch. (g) p-Metal deposition. (h) Proton implantation.

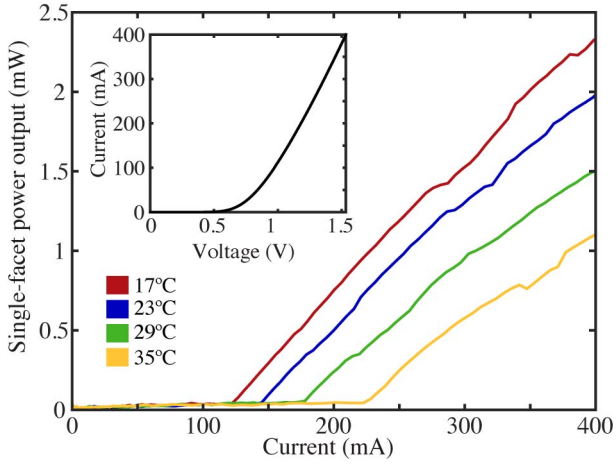

Fig. 4. Light intensity versus current at four temperatures for a device with 2-mm-long mesa, 4-μm-wide current channel, and 1.5-μm-wide silicon waveguide. Inset: current versus voltage for this device at 23°C.

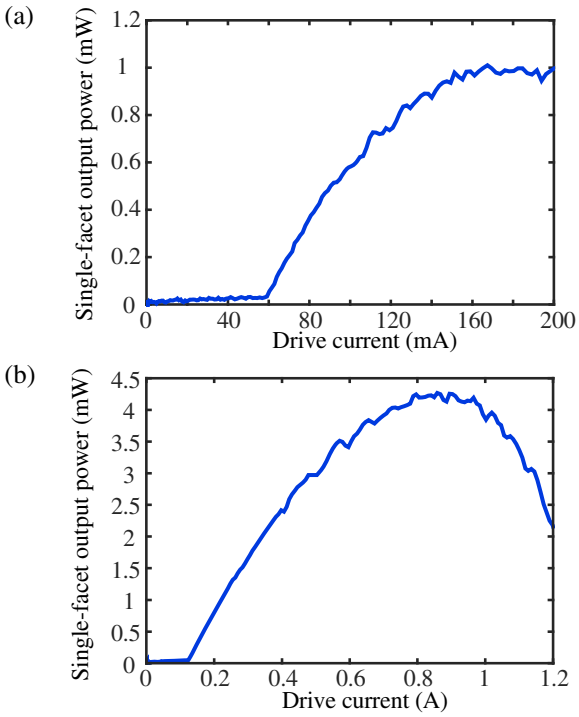

Fig. 5. Light intensity versus drive current for best performing devices. (a) A laser with a 1-mm-long and 6-μm-wide III–V mesa, 4-μm-wide current channel, and 1.5-μm-wide silicon waveguide. The threshold current is 59 mA. (b) A laser with a 2-mm-long and 24-μm-wide III–V mesa, 4-μm-wide current channel, and 2-μm-wide silicon waveguide. The maximum output power is 4.2 mW.

with a 2-mm-long mesa at four temperatures spanning 17°C–35°C. Continuous wave operation was observed up to 26°C and 35°C for devices with 1-mm- and 2-mm-long mesas, respectively. The best performing devices, as shown in Fig. 5, had threshold currents as low as 59 mA and a maximum single-sided output power as high as 4.2 mW at 20°C. The threshold current densities across all devices ranged from about 1280 to 5710 A/cm^2. The histogram in Fig. 6 shows that only 2 of the 50 devices had thresholds exceeding 3600 A/cm^2. Wall plug efficiencies up to 0.6% were measured.

Figures 7 and 8 plot threshold currents and output powers versus silicon waveguide width at 20°C for 2-mm- and 1-mm-long mesas, respectively. The performance variation of lasers with identical design geometries is attributed to fabrication nonuniformity. Of the

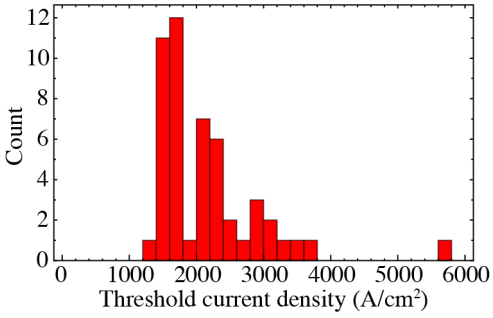

Fig. 6. Histogram of the threshold current density at 20°C for 50 lasers of various geometries.

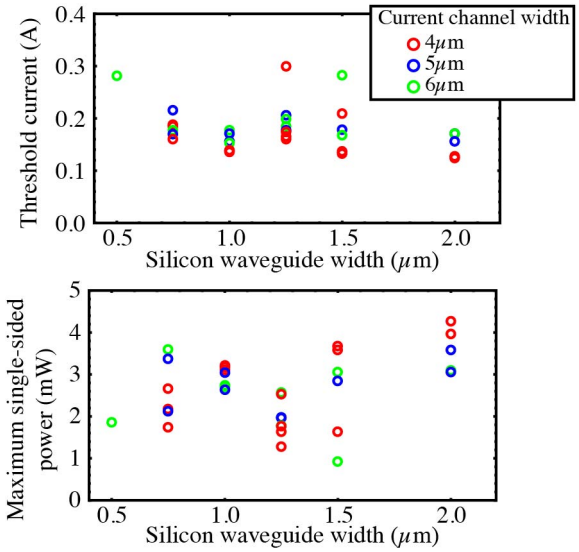

Fig. 7. Dependence of threshold current and maximum single-sided output power on silicon waveguide width for lasers with 2-mm-long III–V mesas.

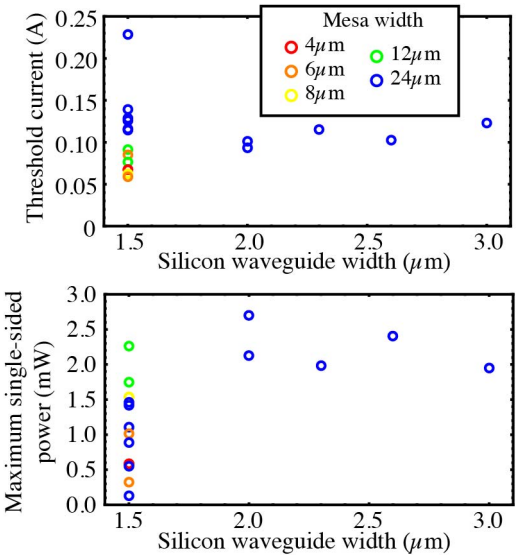

Fig. 8. Dependence of threshold current and maximum single-sided output power on silicon waveguide width for lasers with 1-mm-long III–V mesas.

lasers with 24-μm-wide mesas, those with wider silicon waveguides up to 2 μm performed best overall with lower threshold currents and higher maximum output powers. However, no further improvement was observed when the silicon waveguide width was increased beyond 2 μm. As seen in Fig. 1(b), the mode profile for thinner silicon waveguides extends further laterally from the center of the III–V mesa. While this geometry provides higher total optical confinement in the quantum wells, the modal gain is reduced due to a decreased modal overlap with the carrier density distribution near the center of the mesa. This tradeoff causes a peak net gain value for 2-μm-wide silicon waveguides.

There was no consistent significant correlation between ion-implanted current channel width and device

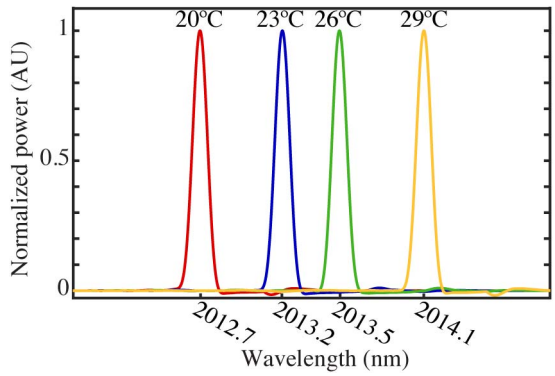

Fig. 9. Normalized optical spectra at various temperatures for a device with a 2-mm-long III–V mesa. Peak wavelengths are indicated on the horizontal axis.

performance; however, the devices with narrow III–V mesas showed the lowest threshold currents. Because the narrow mesa provides improved modal overlap with the carrier density distribution, the modal gain is higher in these devices. However, this improvement over the proton-implanted current channels comes at the expense of reduced thermal dissipation, hence the maximum output power does not improve compared to the wide-mesa design.

The emission spectra were measured by collimating the output and coupling in free space into a Bruker Vertex 70 FT-IR spectrometer. Figure 9 shows the spectra for a 2-mm-long device at four temperatures ranging from 20°C to 29°C. The peak wavelength at 20°C is 2012.7 nm with a FWHM linewidth <0.2 nm, and the wavelength shift with temperature is 0.15 nm/°C. The single-longitudinal-mode behavior is attributed to the tendency of reflections from the III–V tapers to form multiple coupled longitudinal cavities, in addition to the primary lasing cavity defined by the polished silicon facets. In many cases, this caused the devices to lase in a single longitudinal mode, although multiple modes were seen at other drive currents and temperatures. Mode hopping also occurred sometimes as the operating conditions changed. While typically the lasing mode was ≈2.01 μm, different devices and operating conditions produced wavelengths ranging from 1986 to 2033 nm. In future runs, it should be possible to minimize the wavelength nonuniformity by improving both the processing and design of the tapers.

Summarizing, we have demonstrated room temperature, continuous wave, hybrid silicon lasers operating near 2.0 μm, sometimes in a single spectral mode. The devices function up to 35°C, produce up to 4.2 mW of CW single-sided power, have threshold currents as low as 59 mA, and are heterogeneously integrated with silicon waveguides. They are suitable for future integration with wavelength-selective elements such as echelle gratings or arrayed waveguide gratings (AWGs), and photodetectors for compact sensing and detection systems.

The work at both UCSB and NRL is supported by the Office of Naval Research (ONR). This material is based upon work supported by the National Science Foundation Graduate Research Fellowship under Grant No. DGE 1144085. We thank nLight and C. L. Canedy, J. Abell, C. D. Merritt, W. W. Bewley, and C. S. Kim of NRL for useful discussions.

References

1. J. F. Bauters, M. L. Davenport, M. J. R. Heck, J. K. Doylend, A. Chen, A. W. Fang, and J. E. Bowers, Opt. Express **21**, 544 (2013).
2. M. Muneeb, X. Chen, P. Verheyen, G. Lepage, S. Pathak, E. Ryckeboer, A. Malik, B. Kuyken, M. Nedeljkovic, J. Van Campenhout, G. Z. Mashanovich, and G. Roelkens, Opt. Express **21**, 11659 (2013).
3. M. C. Estevez, M. Alvarez, and L. M. Lechuga, Laser Photon. Rev. **6**, 463 (2012).
4. J. G. Crowder, S. D. Smith, A. Vass, and J. Keddie, *Mid-infrared Semiconductor Optoelectronics*, A. Krier, ed. (Springer-Verlag, 2006), pp. 595–613.
5. S. Zlatanovic, J. S. Park, S. Moro, J. M. Chavez-Boggio, I. V. Divliansky, N. Alic, S. Mookherjea, and S. Radic, Nat. Photonics **4**, 561 (2010).
6. X. Liu, R. M. Osgood, Jr., Y. A. Vlasov, and W. M. J. Green, Nat. Photonics **4**, 557 (2010).
7. A. Spott, Y. Liu, T. Baehr-Jones, R. Ilic, and M. Hochberg, Appl. Phys. Lett. **97**, 213501 (2010).
8. R. Shankar, R. Leijssen, I. Bulu, and M. Loncar, Opt. Express **19**, 5579 (2011).
9. A. Malik, M. Muneeb, S. Pathak, Y. Shimura, J. Van Campenhout, R. Loo, and G. Roelkens, IEEE Photon. Technol. Lett. **25**, 1805 (2013).
10. N. Hattasan, B. Kuyken, F. Leo, E. Ryckeboer, D. Vermeulen, and G. Roelkens, IEEE Photon. Technol. Lett. **24**, 1536 (2012).
11. P. Dong, T.-C. Hu, L. Zhang, M. Dinu, R. Kopf, A. Tate, L. Buhl, D. T. Neilson, X. Luo, T.-Y. Liow, G.-Q. Lo, and Y.-K. Chen, Electron. Lett. **49**, 664 (2013).
12. G. Roelkens, U. Dave, A. Gassenq, N. Hattasan, C. Hu, B. Kuyken, F. Leo, A. Malik, M. Muneeb, E. Ryckeboer, D. Sanchez, S. Uvin, R. Wang, Z. Hens, R. Baets, Y. Shimura, F. Gencarelli, B. Vincent, R. Loo, J. Van Campenhout, L. Cerutti, J.-B. Rodriguez, E. Tournié, X. Chen, M. Nedeljkovic, G. Mashanovich, L. Shen, N. Healy, A. C. Peacock, X. Liu, R. Osgood, and W. M. J. Green, IEEE J. Sel. Top. Quantum Electron. **20**, 394 (2014).
13. D. Liang and J. E. Bowers, J. Vac. Sci. Technol. **26**, 1560 (2008).
14. D. Liang, A. W. Fang, H. Park, T. E. Reynolds, K. Warner, D. C. Oakley, and J. E. Bowers, J. Electron. Mater. **37**, 1552 (2008).